True three-dimensional trishear: A kinematic model for strike-slip and oblique-slip deformation

Ernesto O. Cristallini†
Consejo Nacional de Investigaciones Científicas y Técnicas (CONICET–Argentina) and Laboratorio de Tectónica Andina, Departamento de Ciencias Geológicas, Facultad de Ciencias Exactas y Naturales, Universidad de Buenos Aires

Laura Giambiagi
Consejo Nacional de Investigaciones Científicas y Técnicas (CONICET–Argentina)

Richard W. Allmendinger
Department of Earth and Atmospheric Sciences, Cornell University, Ithaca, New York 14853-1504, USA

ABSTRACT

Most structural/kinematic models are inherently two-dimensional; even several recent three-dimensional models are "pseudo–three-dimensional" in that they consist of a series of parallel two-dimensional cross sections. Lack of a true three-dimensional formulation hampers our abilities to simulate three-dimensional structures such as oblique- and strike-slip faulting and displacement gradients perpendicular to the slip vector. The mathematical formulation of trishear deformation using incompressibility of flow is well suited to a solution in three dimensions. We derive one plausible velocity field for true three-dimensional flow in a triangular shear zone. This formulation allows us to simulate the deformation in oblique-slip deformation zones as well as flower structures associated with strike-slip fault zones. The strain distribution in flower structures combined with some simple mechanical assumptions suggests that faults in these zones would have a helicoidal geometry. The results of the kinematic model compare well to well-described structures in the Colorado Plateau, Andaman Sea, and Death Valley, as well as to data from analogue experiments.

Keywords: trishear, strike-slip, numerical model, fault-propagation deformation, oblique-slip, fractures.

INTRODUCTION

A number of mineral deposits and hydrocarbon reservoirs are related to flower structures along strike-slip deformation zones (e.g., Dorsal Neuquina fault system: Vergani et al., 1995; Andaman Sea fault: Harding, 1985; Athos fault: Roussos and Triantafyllos, 1991); in addition, significant earthquake activity along others threatens major population centers (e.g., San Andreas–Garlock system, North Anatolian fault, etc.). Numerous authors have studied this style of deformation, creating a systematic, descriptive classification (Woodcock and Fischer, 1986; Sylvester, 1988; Woodcock and Schubert, 1994). Many field examples (Harding, 1985; Dooley and McClay, 1996; Tindall and Davis, 1999) are well documented, and some analogue and mechanical models have also been presented (Richard and Krantz, 1991; Dooley and McClay, 1996; Dooley and McClay, 1997). However, despite the importance of strike-slip and oblique-slip fault zones, kinematic models to analyze them are virtually unknown because of the inherently three-dimensional nature of the deformation.

During strike-slip analogue experiments the first-formed structures are en echelon Riedel shears. Naylor et al. (1986) have shown that these structures are concave upward and have a helicoidal geometry such that they twist to merge with the principal displacement zone (PDZ) at depth (Naylor et al., 1986; Sylvester, 1988; Woodcock and Schubert, 1994) to form tulip or flower structures. However, it is not theoretically clear why this helicoidal geometry is formed. Naylor et al. (1986) explained it as a consequence of the en echelon pattern of the shears at the surface, their concave-upward geometry, and the need to join a single basement fault at depth.

The three-dimensional arrangement of these structures suggests the possibility that they have been formed in a triangular deformation zone where the apical line is the upper termination of the main fault (Fig. 1B). Here we present a novel application of the trishear kinematic model—initially proposed by Erslev (1991), later extended by Hardy and Ford (1997) and Zehnder and Allmendinger (2000)—that can be used to simulate the structure of strike-slip and oblique-slip deformation. Because Erslev's (1991) method is inherently two-dimensional, we first derive a three-dimensional solution based on incompressibility of flow. A computer program was written to apply this solution, and the results were compared with natural examples and analogue models.

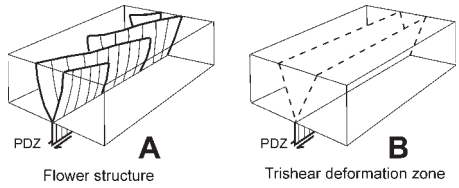

Figure 1. (A) Helicoidal geometry of Riedel faults (Naylor et al., 1986). PDZ—principal displacement zone. (B) Concept of trishear applied to strike-slip deformation.

The kinematic model that we present here is a true three-dimensional generalization of the trishear-model velocity field presented by Zehnder and Allmendinger (2000) and differs from Cristallini and Allmendinger's (2001) pseudo–three-dimensional approximation. Although the new model is in some ways less versatile than the pseudo–three-dimensional approach, it is much more powerful for successfully simulating oblique and strike-slip deformation.

†E-mail: ernesto@gl.fcen.uba.ar.

GSA Bulletin; July/August 2004; v. 116; no. 7/8; p. 938–952; doi: 10.1130/B25273.1; 15 figures.

IMPLEMENTATION OF THREE-DIMENSIONAL TRISHEAR ALGORITHM

The bedding is defined in the model by a rectangular array of up to 200 by 200 points. The fault is a plane that delimits two different blocks and could be vertical or have any inclination. The moving block is always the hanging wall, and if the fault is dipping 90° (vertical), the hanging wall is defined arbitrarily. The total slip specified for the moving block is applied in incremental steps. Three fields of motion, labeled A, B, and C (Fig. 2A), are defined. Field A is in the moving block of the fault (hanging wall), B corresponds to the trishear zone, and C is the stationary block (footwall) of the fault. In each step of displacement, points are moved at a constant velocity parallel to the fault if they are located in field A or moved according to the following velocity description of three-dimensional trishear if they are in field B. All points in the footwall (field C) are held stationary.

We define two right-handed coordinate systems: The first is a "geographic system" in which X' (east) and Y' (north) are horizontal, and perpendicular and parallel, respectively, to the strike of the initial fault tip-line. Z' is vertical and positive upward (Fig. 2C). The deformation zone defines the second coordinate system, where X is perpendicular to the tip-line and contained in the fault plane (positive forward), Z is the tip-line (also contained in the fault plane), and Y is perpendicular to the fault plane and positive toward the moving block (Figs. 2B and 2C).

To implement true three-dimensional trishear, we apply the condition of flow incompressibility inside the deformation zone, specified by setting the divergence of the velocity field (div v) to zero (Mase and Mase, 1992). Zehnder and Allmendinger (2000) used this condition for the two-dimensional trishear model, but here we also consider flow in the Z direction:

$$\operatorname{div} v \equiv \frac{\partial V_x}{\partial x} + \frac{\partial V_y}{\partial y} + \frac{\partial V_z}{\partial z} = 0 \qquad (1)$$

V_x, V_y, and V_z are the velocities in the directions X, Y, and Z of the deformation-zone–defined coordinate system, and x, y, and z are the distances of the point in question along the respec-

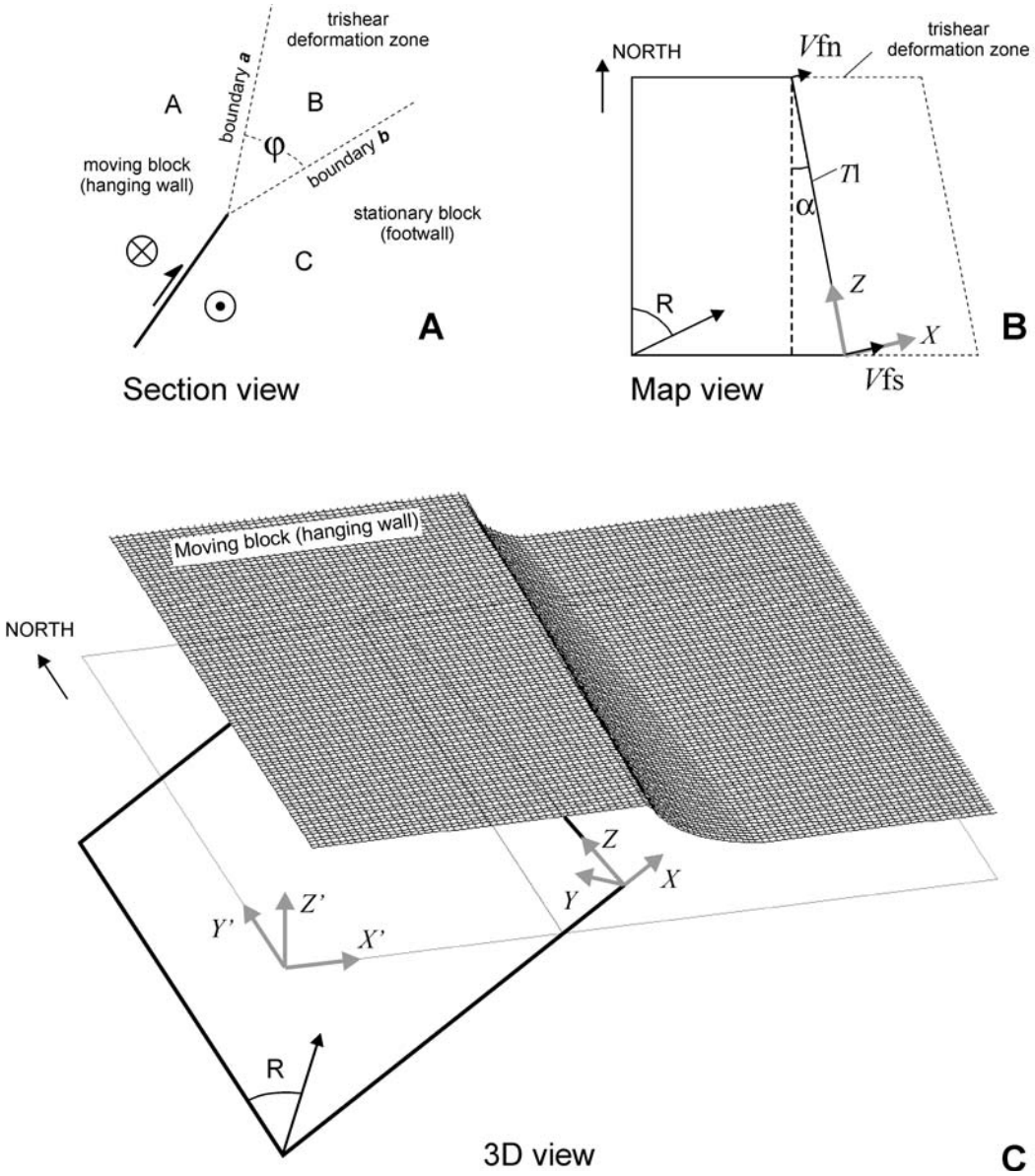

Figure 2. Coordinate systems used in three-dimensional trishear. A dipping fault was chosen to indicate the most general situation. (A) Section view of fault propagation and motion fields used (see text for reference). (B) Map view of the fault plane. (C) Three-dimensional view of the fault-fold system where both coordinate systems used are indicated. In nonvertical faults, the moving block is always the hanging wall. In vertical faults, the moving block is arbitrarily chosen and identified as the hanging wall. Vfn and Vfs are the velocities at the "northern" and "southern" ends of the hanging wall, and Tl is the length of the tip-line inside the model.

tive directions. We postulate velocity fields for V_x and V_z, and we calculate the V_y velocity field.

Zehnder and Allmendinger (2000) showed that an infinite number of velocity fields that conserve cross-sectional area can be applied within the two-dimensional trishear zone. However, the simple linear field has been shown to fit many structures well (Hardy and Ford, 1997) and is reasonable in light of mechanical analyses (Cardozo et al., 2003). In three dimensions, the number of volume-conserving velocity fields is likewise infinite. The three-dimensional trishear presented in this paper is only one of the simplest of those velocity fields.

In the algorithm proposed, we permit linear changes in velocity and trishear angle along the *Z* axis (the simplest, but not unique case). To achieve the first change, the velocity of any particle of the hanging wall of the fault (V_f) in the *X*, *Y*, *Z* coordinate system is defined by the linear equation

$$V_f = (A_v \times z) + V_{fs}, \quad (2)$$

where V_{fs} is the velocity in the "southern" border of the (Fig. 2B) moving block and A_v is given by

$$A_v = \frac{V_{fn} - V_{fs}}{T_l},$$

where V_{fn} is the velocity at the "northern" border of the moving block and T_l is the length of the tip-line inside the model. T_l may change during the simulation.

Linear variations of the trishear angle (φ) through the *Z* direction are expressed by (Fig. 2A)

$$\varphi = (A_t \times z) + \varphi_s, \quad (3)$$

where φ_s is the trishear angle in the southern border of the model and A_t is given by

$$A_t = \frac{\varphi_n - \varphi_s}{T_l},$$

where φ_n is the trishear angle in the northern border of the model. A_v, V_{fs}, A_t, and φ_s can change at any stage of movement.

In the border between the deformation zone (trishear zone) and the moving block or hanging wall (boundary *a* of Fig. 2A), the boundary conditions are

$$V_{a,x} = V_f \sin(R + \alpha)$$
$$V_{a,y} = 0 \quad (4)$$
$$V_{a,z} = V_f \cos(R + \alpha),$$

where $V_{a,x}$, $V_{a,y}$, and $V_{a,z}$ are the velocity components of any particle on boundary *a* (Fig. 2A), defined by

$$y = x \tan \varphi.$$

R is the rake of the velocity vector in the hanging wall, measured from the north (Figs. 2B and 2C), and α is the angle that the tip-line has rotated from its initial position measured over the fault plane.

In the border between the deformation zone and the stationary block or footwall (boundary *b* of Fig. 2A), the boundary conditions are

$$V_{b,x} = 0$$
$$V_{b,y} = 0 \quad (5)$$
$$V_{b,z} = 0,$$

where $V_{b,x}$, $V_{b,y}$, and $V_{b,z}$ are the velocity components of any particle on the boundary *b* (Fig. 2A), defined by

$$y = -x \tan \varphi.$$

Inside the deformation zone, we assume the simplest case or "linear field" where V_x and V_z vary linearly in the *Y* direction. This relationship is given by

$$V_x = \frac{V_{a,x}}{2}\left[\frac{y}{x \tan \varphi} + 1\right] \quad (6)$$

$$V_z = \frac{V_{a,z}}{2}\left[\frac{y}{x \tan \varphi} + 1\right], \quad (7)$$

and we will use equation 1 to find V_y. The *x* term of equation 1 is easy to find by differentiating equation 6:

$$\frac{\partial V_x}{\partial x} = -\frac{V_{a,x}}{2} \cdot \frac{y}{x^2 \tan \varphi} \quad (8)$$

However, to derive the *z* term of equation 1, we have to work a little harder. We use equations 2, 3, and 4 to rewrite equation 7 as

$$V_z = \frac{\left[(A_v \times z) + V_{fs}\right]\cos(R + \alpha)}{2}\left[\frac{y}{x \tan\left[(A_t \times z) + \varphi_s\right]} + 1\right], \quad (9)$$

and to simplify equation 9, we write

$$V_z = A(z) \times B(z), \quad (10)$$

where

$$A(z) = \frac{\left[(A_v \times z) + V_{fs}\right]\cos(R + \alpha)}{2} \quad (11)$$

$$B(z) = \left[\frac{y}{x \tan\left[(A_t \times z) + \varphi_s\right]} + 1\right]. \quad (12)$$

Differentiating equation 10 yields

$$\frac{\partial Vz}{\partial z} = A'(z) \times B(z) + A(z) \times B'(z), \quad (13)$$

where $A'(z)$ and $B'(z)$ are the differentiates of equations 11 and 12, respectively:

$$A'(z) = \frac{Av \times \cos(R + \alpha)}{2} \quad (14)$$

$$B'(z) = -\frac{y}{z} J(z), \quad (15)$$

and $J(z)$ is used to simplify the writing of equation 15

$$J(z) = \frac{1}{\tan^2\left[(A_t \times z) + \varphi_s\right]\cos^2\left[(A_t \times z) + \varphi_s\right]}. \quad (16)$$

Now, we have two terms of equation 1 (the *x* and *z* terms: equations 8 and 13, respectively), and we can calculate the third one (the *y* term). Rearranging equation 1 yields

$$\frac{\partial V_y}{\partial y} = -\frac{\partial V_x}{\partial x} - \frac{\partial V_z}{\partial z}, \quad (17)$$

and by using equations 8, 11, 12, 13, 14, 15, and 16, we can rewrite equation 17:

$$\frac{\partial V_y}{\partial y} = \frac{V_{a,x} \times y}{2x^2 \tan\left[(A_t \times z) + \varphi_s\right]} - A'(z)\left[\frac{y}{x \tan\left[(A_t \times z) + \varphi_s\right]} + 1\right] + \left[A(z) \times J(z)\frac{y}{z}\right]. \quad (18)$$

Integrating equation 18 finally allows us to obtain V_y:

$$V_y = \frac{V_{a,x} \times y^2}{4x^2 \tan\left[(A_t \times z) + \varphi_s\right]} - \left[\frac{A'(z) \times y^2}{2x \tan\left[(A_t \times z) + \varphi_s\right]}\right] - A(z) + \frac{^2A(z) \times J(z) \cdot y}{2x} + C, \quad (19)$$

where the constant of integration is

$$C = \frac{V_{a,x}}{4}\tan\left[(A_t \times z) + \varphi_s\right] + \frac{A'(z) \times \tan\left[(A_t \times z) + \varphi_s\right]}{2} + A'(z) - \frac{A'(z) \times \tan^2\left[(A_t \times z) + \varphi_s\right] \times J(z)}{2}.$$

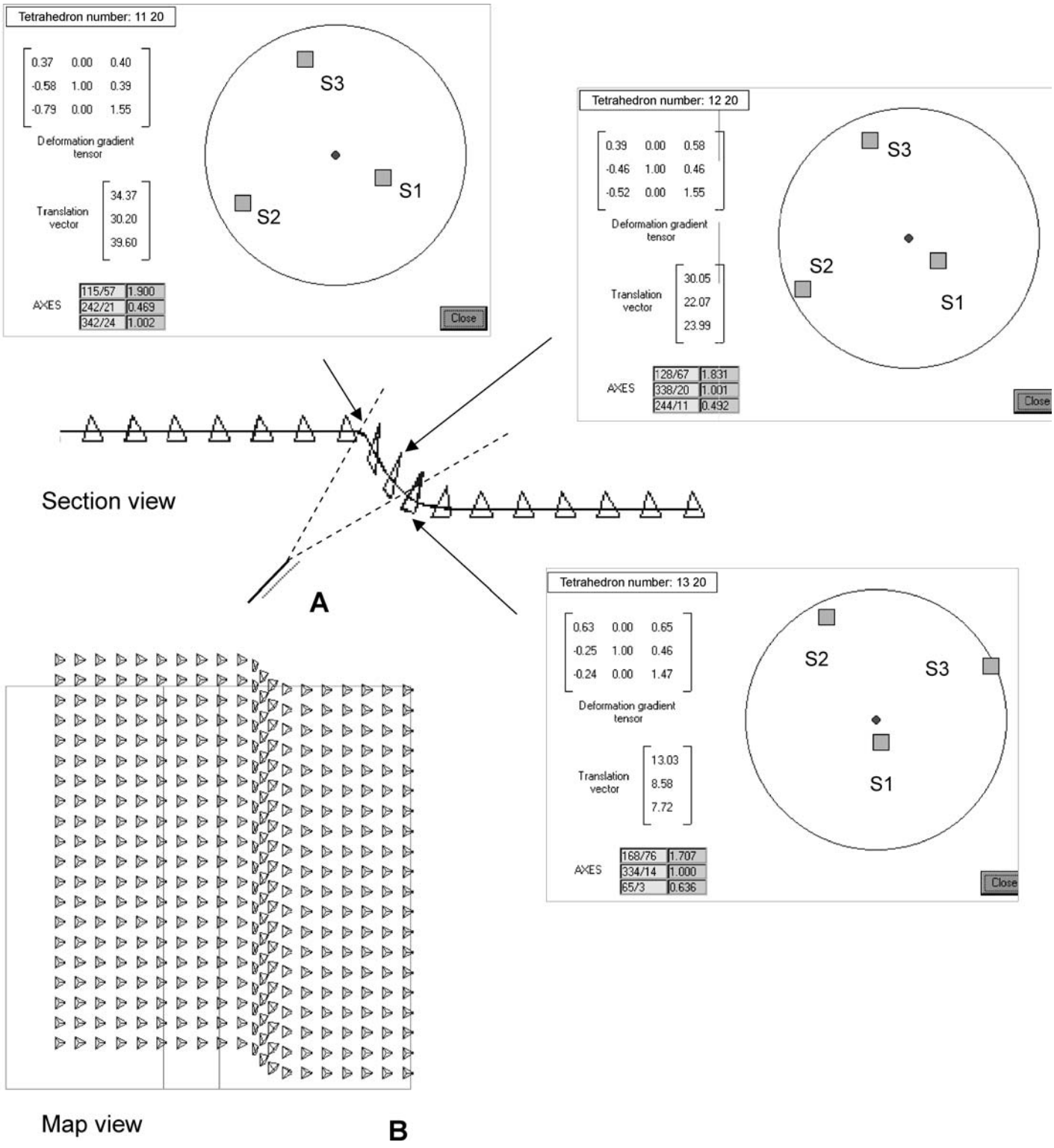

Figure 3. Strain analysis using tetrahedrons in an oblique-slip three-dimensional trishear deformation. The deformation-gradient tensor and the translation vector can be calculated for any three-dimensional position. The orientations and lengths of the principal axes can be derived (see discussion in text). (A) Section view of the model. (B) Map view of the model. Each box is a window of the program showing the information for a specific tetrahedron (as shown by the arrows), where the circle is a stereographic projection of the principal strain axes (S1—maximum, S2—intermediate, S3—minimum).

From the above equations we can calculate the velocities V_x, V_y, and V_z of a point for which x, y, and z are known. A coordinate transformation must have been performed previously to convert from geographic coordinates x', y', and z'.

STRAIN ANALYSIS

Several authors have already begun to explore the mechanics of two-dimensional trishear models (Johnson and Johnson, 2002; Cardozo et al., 2003; Finch et al., 2003). However, three-dimensional trishear is only a kinematic model, and no mechanics are involved. Because of this fact, the fracture prediction proposed here is only an approximation and has to be used with caution.

For homogeneous deformation, the relative displacements of the four points of an initially equilateral tetrahedron are sufficient to define the strain ellipsoid (Williams and Kane, 1999). As the use of a tetrahedron results in a far more efficient calculation than displacing an array of points defining an initial sphere, we draw on this method to track the strain in our models (Fig. 3). Each point of the tetrahedron is moved by using the three-dimensional trishear velocity field defined above. For visualization, a stereonet plot displays the three principal strain axes determined from each deformed tetrahedron, and the orientation and relative length of each axis are displayed (Fig. 3). We use small tetrahedra so that the strain within the region circumscribed by the nodes is more or less homogeneous. Prediction of deformation intensity using the relationships between length of axes could be done for any three-dimensional position inside the model. At small displacements, the modeled strain (finite strain) axes approximate those of the infinitesimal strain ellipsoid. Under the assumption that in this case the stress and strain ellipsoids are coaxial, we can use a simple Mohr-Coulomb failure criterion or a more complex three-dimensional fracture analysis such as that proposed by Reches (1978) to predict shear and tensile fractures of the model. In all the examples used in this paper, we assume 30° as the internal friction angle.

CHANGES IN VARIABLES ALONG STRIKE

For the changing of variables along strike, our true three-dimensional trishear is less versatile than the pseudo–three-dimensional trishear described by Cristallini and Allmendinger (2001). For example, no changes in the fault angle are permitted along strike because they would produce a curvilinear coordinate axis Z and would complicate the boundary conditions. Slip, trishear angle, and P/S (propagation to slip ratio) can change without problems along strike. Currently, we have addressed only a linear variation of these parameters along strike, but the algorithms could easily be adapted to more complicated variations.

Slip Variation

Slip variations along strike can be evaluated by the three-dimensional trishear equations. However, if any obliquity is applied (rake different from 90°) and the model is partially analyzed, the volume of the moving block (hanging wall) and the trishear zone will change. As an example of this scenario, we can use the model of Figure 4 where a right-lateral, strike-slip fault dipping 90° is represented. The model in Figure 4A shows the western termination where the fault passes eastward from zero displacement in the west to a 10 "program units" displacement in the fault's center. The model in Figure 4B shows the eastern termination of the same fault where the fault passes eastward from a 10-unit displacement in the fault's center to zero displacement in the east. If we analyze both models separately, we will find that the eastern one (Fig. 4B) loses volume in the moving block (northern block: in this case [a vertical fault] arbitrarily defined as the hanging wall) and the trishear zone, whereas the western one (Fig. 4A) gains volume. A model composed by both parts (Figs. 4A and 4B) will conserve volume, but this situation implies a nonrigid hanging-wall translation and of course a nonrigid trishear zone. Even in cases where slip variation is not symmetric, as it is in Figure 4, the volume will be conserved if we consider the whole fault from tip-line to tip-line. These cases are like applying a homogeneous pure shear throughout the hanging wall. Usually, field examples show some minor structures such as the "horsetail" pattern of oblique and perpendicular folds and faults that accommodate the hanging-wall deformation at the termination of a strike-slip fault.

To analyze deformation inside the trishear zone, we use the tetrahedron method in the same example as in Figure 4 but apply a very small maximum displacement (1 program unit) just to model an infinitesimal strain (Fig. 5A). The variation of strain axes along the strike of the fault are plotted in stereographic projections (Fig. 5B) for a path inside the trishear zone placed near the north boundary of it (scan

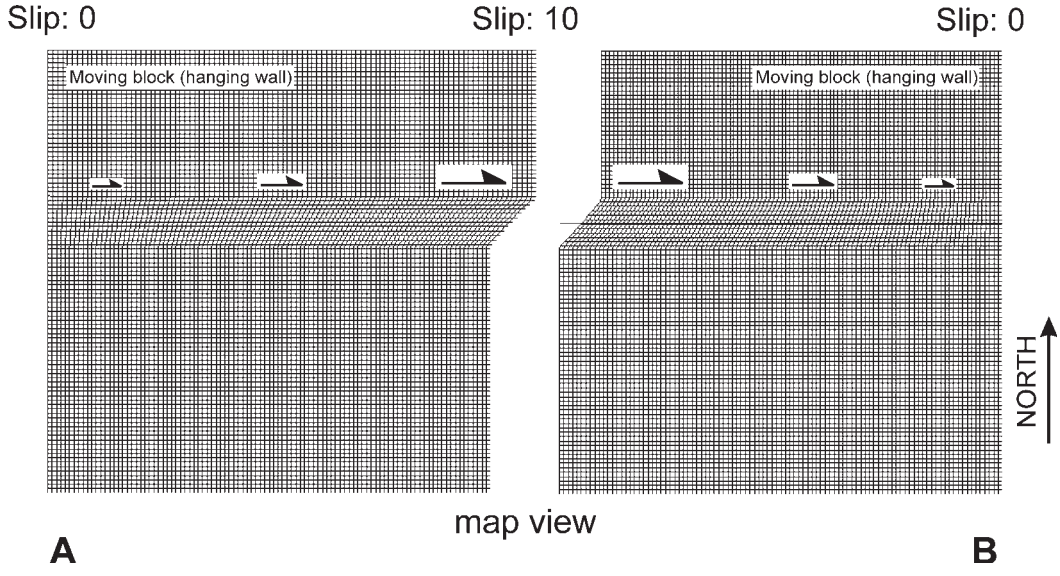

Figure 4. Map view of a trishear model of a vertical, east-striking, right-lateral, strike-slip fault. The hanging wall (moving block) is arbitrarily defined as the northern block. The slip of the hanging wall changes along strike from (A) zero in the west to 10 program units in the center to (B) zero again in the east. A constant *P/S* of 1.5 and trishear apical angle of 30° was used. The volume is conserved; see discussion in text.

line in Fig. 5A). The shear-fracture orientation—calculated under the assumptions that a Mohr-Coulomb failure criterion applies and that stress and infinitesimal strain are coaxial (see section on Strain Analysis, above)—are also drawn in stereographic projections (Fig. 5C).

The intermediate strain axis (S2) will be fixed and placed near the vertical position (it will be vertical only over the fault tip-line), whereas maximum and minimum axes (S1 and S3) will rotate near the horizontal plane. This rotation is faster near the west and east fault terminations than in the middle of the model. Likewise, the orientations of the Riedel fractures (R1 and R2) are almost constant in the middle of the model but change very abruptly in both extremes. The magnitude of the strain axes changes linearly. S1 changes from 1 in the west to 1.1 in the center and to 1 again in the east. S3 is 1 in the west, 0.9 in the center, and 1 again in the east. S2 magnitude will be constant along strike. The horizontal projection of the tension fractures predicted by the model is plotted in Figure 5A inside the trishear zone. Both terminations show a pattern of tension fracture strikes that resemble the leading and trailing extensional imbricate fans (Figs. 5D and 5E) described by Woodcock and Fischer (1986).

Trishear-Angle Variation

The thickness of the deformation zone associated with a fault could change as a function of the rheology of the rocks involved (Finch et al., 2003). For example, a lateral change in facies of sedimentary rocks could produce changes in deformation thickness along the strike of a fault. Variation in trishear angle along strike can

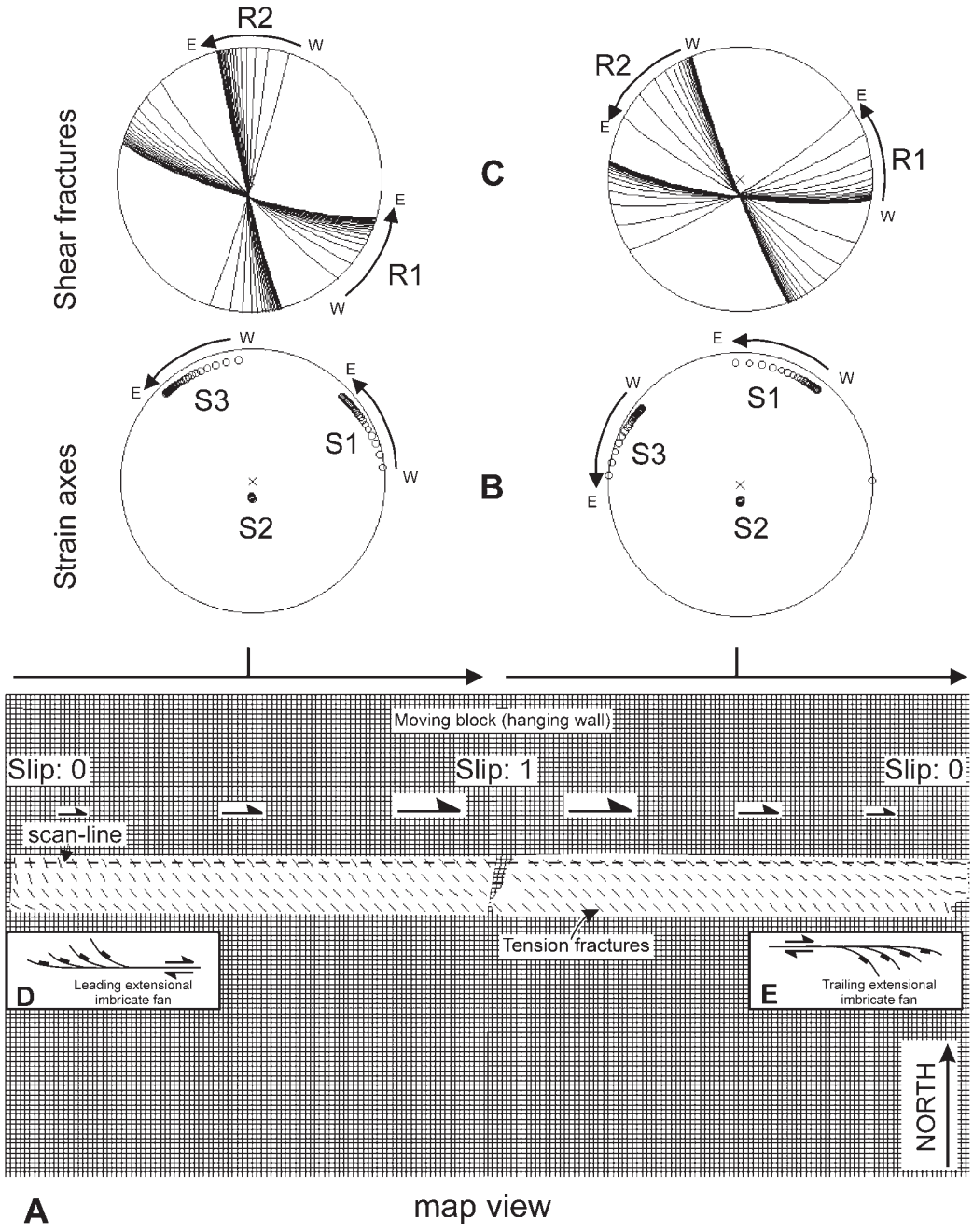

Figure 5. (A) Map view of a trishear model of a vertical, east-striking, right-lateral, strike-slip fault. The hanging wall (moving block) is arbitrarily defined as the northern block. The slip changes along strike from zero in the west to one program unit in the center and to zero again in the east. The strain inside the trishear zone was analyzed through a line parallel to the fault (scan line shown in gray dashes) near the northern boundary of the trishear zone. (B) Stereographic projections showing the evolution through strike (E—east, W—west) of the principal infinitesimal strain axes calculated by the model (S1—major, S2—intermediate, and S3—minimum). (C) Stereographic projections showing the evolution through strike (E—east, W—west) of the shear fractures predicted by the model (R1—Riedel 1 fractures and R2—Riedel 2 fractures). The horizontal projection of predicted tension fractures are plotted in a map view in A inside the trishear zone. (D and E) Leading and trailing extensional imbricate fans (Woodcock and Fischer, 1986) are showed (see discussion in text).

be used to simulate such changes and can be made without any volume problem in the three-dimensional model.

Figure 6 shows an example of a vertical, strike-slip fault with a variation of the trishear angle between 80° in the south and 10° in the north. The map projections of possible extensional (Fig. 6A) and Riedel (Fig. 6B) fractures are plotted, where the fractures were calculated as explained above. Figure 6C shows the evolution of the infinitesimal strain axes through the arrow drawn in Figures 6A and 6B. Figures 6D and 6E show the evolution of extensional and Riedel fractures through the same arrow. The major strain axis (S1) plunges to the northwest in the western side of the trishear and to the southeast in the eastern side and tends to be horizontal in the middle of the trishear zone. The minor strain axis (S3) plunges to the northeast in the western side of the trishear zone and to the southwest in the eastern side, but tends to be horizontal in both boundaries of the trishear zone. The intermediate strain axis (S2, near the vertical) traces a path from southeast (in the west) to southwest (in the east). The strikes of both extensional and Riedel fractures are predicted to be more parallel to the fault to the east, and both types of fractures are predicted to dip to the east in the west and to the west in the east. If we analyze these rotations for the northern part of the trishear zone, we will find the same pattern, but it will change across a short distance as the trishear zone is thinner to the north.

Figure 6F shows a deformation map of the model where S1/S3 is represented in gray scale.

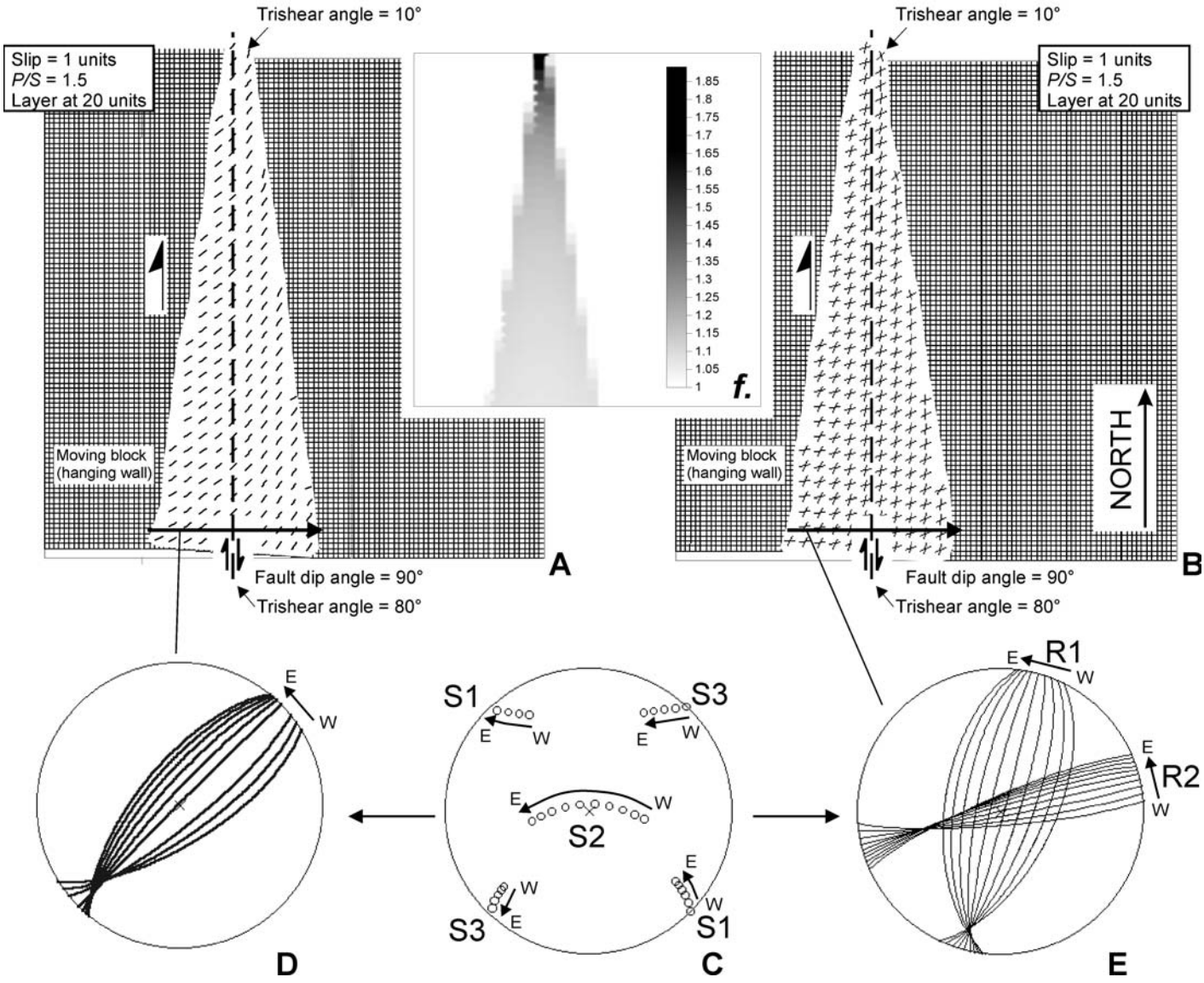

Figure 6. Deformation results of three-dimensional trishear with apical-angle variation along strike over a vertical, north-striking, right-lateral fault. The hanging wall (moving block) is arbitrarily defined as the western block. (A) Horizontal projection of possible extensional fractures. (B) Horizontal projection of possible Riedel fractures. (C) Evolution of the principal infinitesimal strain axes (S1—major, S2—intermediate, and S3—minimum) through the arrow drawn in A and B. (D and E) Evolution of the extensional and Riedel fractures (R1—Riedel 1 fractures and R2—Riedel 2 fractures) through the same arrow drawn in A and B. (F) Deformation map representing the S1/S3 ratios.

Note how the deformation is more intense where the trishear zone is more constricted.

Variation in *P*/*S* (Propagation to Slip) Ratio

In the three-dimensional trishear model proposed in this paper, the *P*/*S* ratio is measured parallel to the slip vector of the moving block (hanging wall) but not necessarily perpendicular to the tip-line. In fact, it will be parallel to the tip-line only in a strike-slip case, and it will be perpendicular to the tip-line in a dip-slip case. This geometry means that in a strike-slip deformation, the only propagation permitted by this model is lateral; nevertheless, vertical propagation can be achieved by oblique-slip or dip-slip deformation.

Variations of *P*/*S* ratio along strike can be applied in the numerical model without any problem but is only important in dip-slip and oblique-slip deformation. Variations of *P*/*S* ratio have no effect in strike-slip cases because the fault is considered infinitely long, so lateral propagation will only propagate the fault over itself and, of course, any variations of *P*/*S* along strike make no sense and have no effect in this case.

The geometric effects of *P*/*S* variation in the three-dimensional trishear deformation of dip-slip and oblique-slip faults are similar to those described by Cristallini and Allmendinger (2001) in the pseudo–three-dimensional trishear. Such effects imply folds that evolve from a gently dipping to a steeply dipping or overturned forelimb and from a blind thrust to an emergent fault owing to the change in tip-line position along strike.

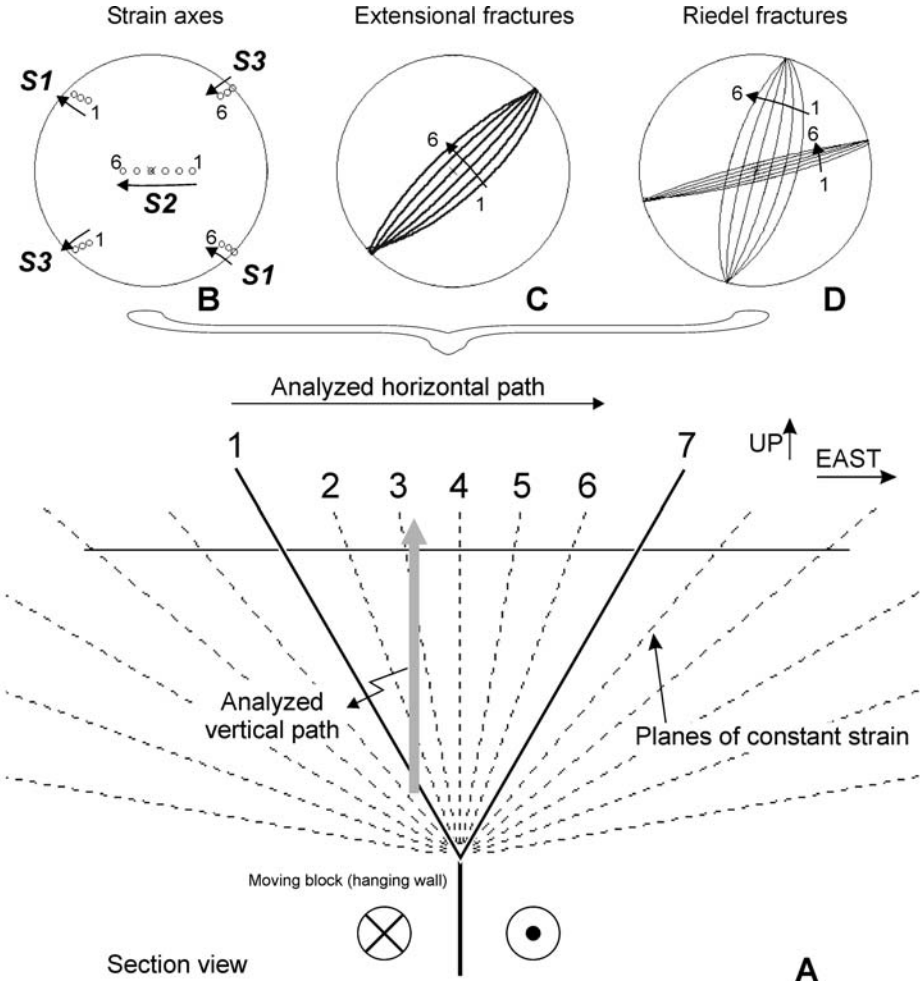

Figure 7. (A) Cross section of a vertical, right-lateral, strike-slip trishear model with apical angle of 60°. The hanging wall (moving block) is arbitrarily defined in the western block. A very small displacement was applied to simulate infinitesimal deformation. The dashed lines indicate planes of constant strain (see discussion in text). (B–D) Stereographic projections of the predicted strain-ellipsoid axes and extensional and Riedel fractures for planes 1 to 6 of A. The vertical path shown by a gray arrow in A is analyzed in the text and Figure 8.

STRIKE-SLIP ANALYSIS

A simple strike-slip example with constant parameters along strike was analyzed to investigate the deformation within the trishear zone. The predicted Riedel and extension-fracture orientations were calculated for a vertical path and a horizontal path through the model.

The example chosen is a vertical, right-lateral, strike-slip fault with a trishear angle of 60° (Fig. 7A). A very small displacement was applied to simulate infinitesimal deformation and derive the predicted fracture orientations by using Coulomb-Mohr theory with an internal friction angle of 30°. The moving block was arbitrarily selected to the left of the fault and called the hanging wall in this example. Because all the variables of trishear are constant along strike, we can define planes of constant deformation inside the triangular zone that contain the tip-line (Fig. 7A). Any point in one of these planes has the same strain ellipsoid and the same predicted fractures. Analyzing the deformation from the hanging wall to the footwall (from west to east in Fig. 7A), we can see that all of the predicted fractures incline toward the strike-slip fault (the PDZ) and are vertical in the middle of the trishear zone (Figs. 7C and 7D). The major axis (S1) of the strain ellipsoid is almost horizontal and has an azimuth of 135°, whereas the minor axis (S3) is also horizontal and has an azimuth of 045°, and the intermediate axis (S2) is approximately vertical (see path in Fig. 7B).

As we analyze the deformation in a vertical line through the trishear zone, we cut across the planes of constant strain mentioned before. For example, along the path marked with a thick gray line in Figure 7A, we crosscut planes 1, 2, and 3, and the predicted fracture angle increases upward. This is a reasonable simulation of the section view of a flower (tulip) structure. In Figure 8, the propagation of an extensional fracture from the PDZ is shown in a cross section. Note that the dip angle of extensional fractures in each plane of constant strain (dashed lines in Fig. 8) is larger than the dip of the plane itself. This geometry means that if a fracture grows from the PDZ, it will cut up the lines of constant strain, and the dip angle will increase upward. Such fracture, therefore, results in a curved and upwardly concave shape. Figure 9 shows the growth of a predicted extensional fracture from the middle of the trishear zone. The progressive evolution of extensional fractures through planes of constant strain would result in a helicoidal shape (Fig. 1A), as described by Naylor et al. (1986).

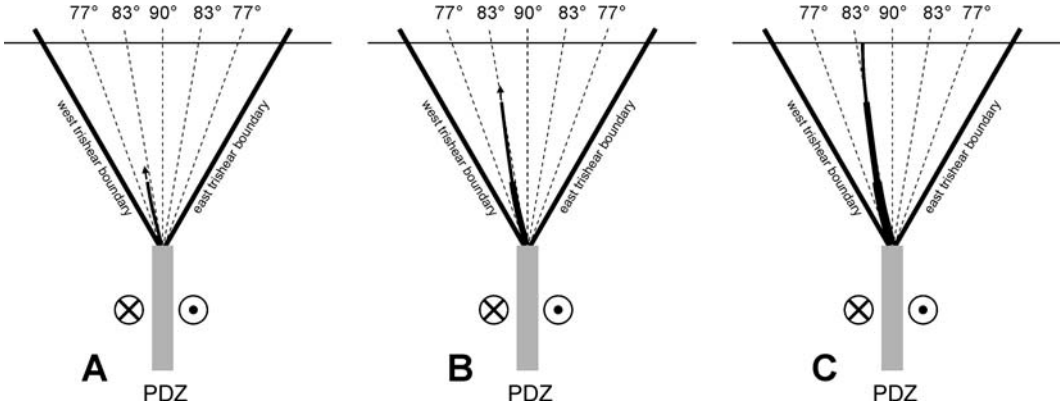

Figure 8. Cross section of the same example as Figure 7, showing the growth through time (A to C) of an extensional fracture (near the 83° line on the left) emanating from the principal displacement zone (PDZ). Dashed lines indicate section view of planes of constant strain; the numbers indicate the dipping angle of extensional fractures in each plane. Note the curved shape and upward concavity of the fracture.

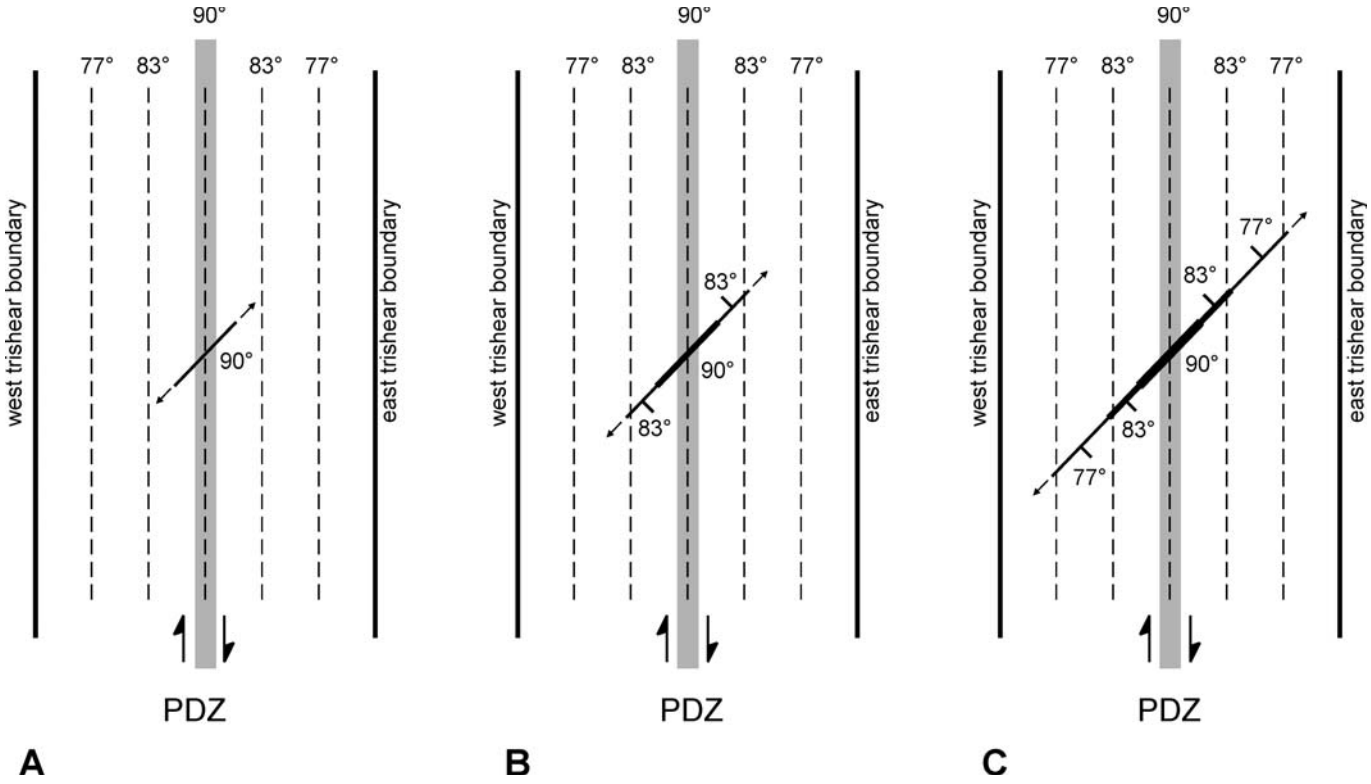

Figure 9. Map view of the same example as Figures 7 and 8, showing the growth through time of an extensional fracture from the middle of the trishear zone. Dashed lines indicate map view of planes of constant strain; the numbers indicate the dip angle of extensional fractures in each plane. Note the helicoidal shape acquired by the fracture.

Similar shapes will result if we model Riedel instead of extensional fractures.

This simple description is valid only for a simple strike-slip case. If, for example, we change the trishear apical angle along the strike of the fault, the above-described planes of constant strain will be converted to curved surfaces of constant strain, and the fracture and deformation analysis would be more complicated.

COMPARISON WITH NATURAL EXAMPLES

Here, we compare the geometries obtained from applying the three-dimensional trishear numerical model to three natural examples. The first example is a compressional strike-slip system; the second and third cases are negative and positive flower structures, respectively.

Example 1: East Kaibab Monocline, Colorado Plateau, United States

In the northern 50 km of the East Kaibab monocline of the Colorado Plateau, a N20°E-trending, monocline-parallel zone of intense deformation is expressed by abundant faults and fractures (Tindall and Davis, 1999). Tindall and Davis (1999) demonstrated that

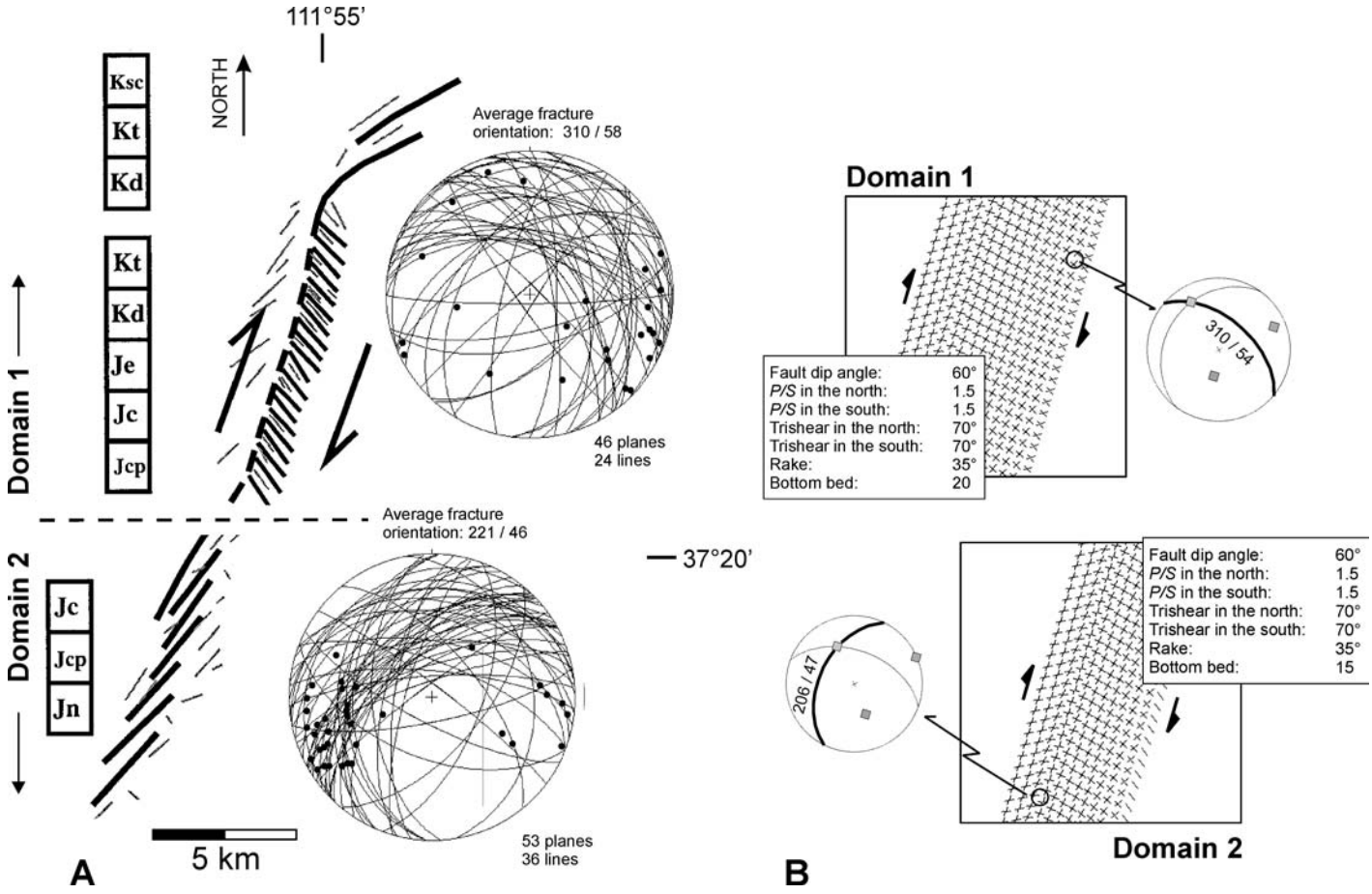

Figure 10. (A) Main structures of domains 1 and 2 of the East Kaibab monocline in the Colorado Plateau, United States (from Tindall and Davis, 1999). Jurassic (J) and Cretaceous (K) stratigraphic intervals cropping out in each domain are indicated. Stereographic projections of slip surfaces and slickenlines are shown. (B) Three-dimensional trishear models with bottom beds at 20 and 15 program units, respectively, which resemble the progressively higher stratigraphic intervals from domain 1 to domain 2.

a significant clockwise strike-slip component acted together with a reverse dip-slip movement during the formation of this structure. These authors subdivided the monocline into four domains on the basis of style of deformation and outcropping stratigraphic intervals. Domains 1 and 2 have been chosen as a field test for the three-dimensional trishear model (Fig. 10A). Domain 1 occupies the stratigraphic interval of Jurassic through Cretaceous strata and is affected by northwest-striking, northeast-dipping faults. Average strike and dip of faults are N50°W, 58°NE, and slickenlines rake 20°SE, suggesting left-lateral slip with a small reverse component. Deformation of domain 2 is in a slightly lower stratigraphic interval and is marked by northeast-striking faults with average orientation N41°E, 46°NW and slickenlines raking ~30°SW.

The principal basement fault is not exposed in these domains, so we assume a 60° fault dip. The rake (35°) was acquired by the ratio of strike slip to dip slip given by Tindall and Davis (1999). The trishear angle (70°) was obtained from the width of the deformation area and the thickness of the sedimentary cover. The stratigraphic level cropping out in each domain, Cretaceous in the north and Jurassic in the south, can be modeled by modifying the level of bed grid in the model.

Domain 1 northwest-striking, northeast-dipping faults can be correlated with the eastern Riedel 2 shears obtained with the three-dimensional trishear model (Fig. 10B). Both the fault strike and dip are reasonably matched. The domain 2 northeast-striking, northwest-dipping faults with reverse and right-lateral offsets have been plausibly simulated by the western Riedel 1 shears of the model (Fig. 10B).

Example 2: Andaman Sea

The Andaman Sea is a marginal basin dominated by extensional deformation related to a northeast-trending spreading ridge (Harding, 1985). A major north-northwest–striking wrench fault with normal offset has been interpreted by Harding (1985) as a regional-basement tear fault defining a negative flower structure (Fig. 11). The region is dominated by several oblique normal faults that flank the principal wrench fault. Close to this fault, two types of folds are present: (1) forced folds parallel to the wrench fault, thought to be caused by dip-slip components of the displacement because they resemble the forced folds that are formed at the upthrown edge of normal-fault blocks, and (2) folds that result from lateral shortening.

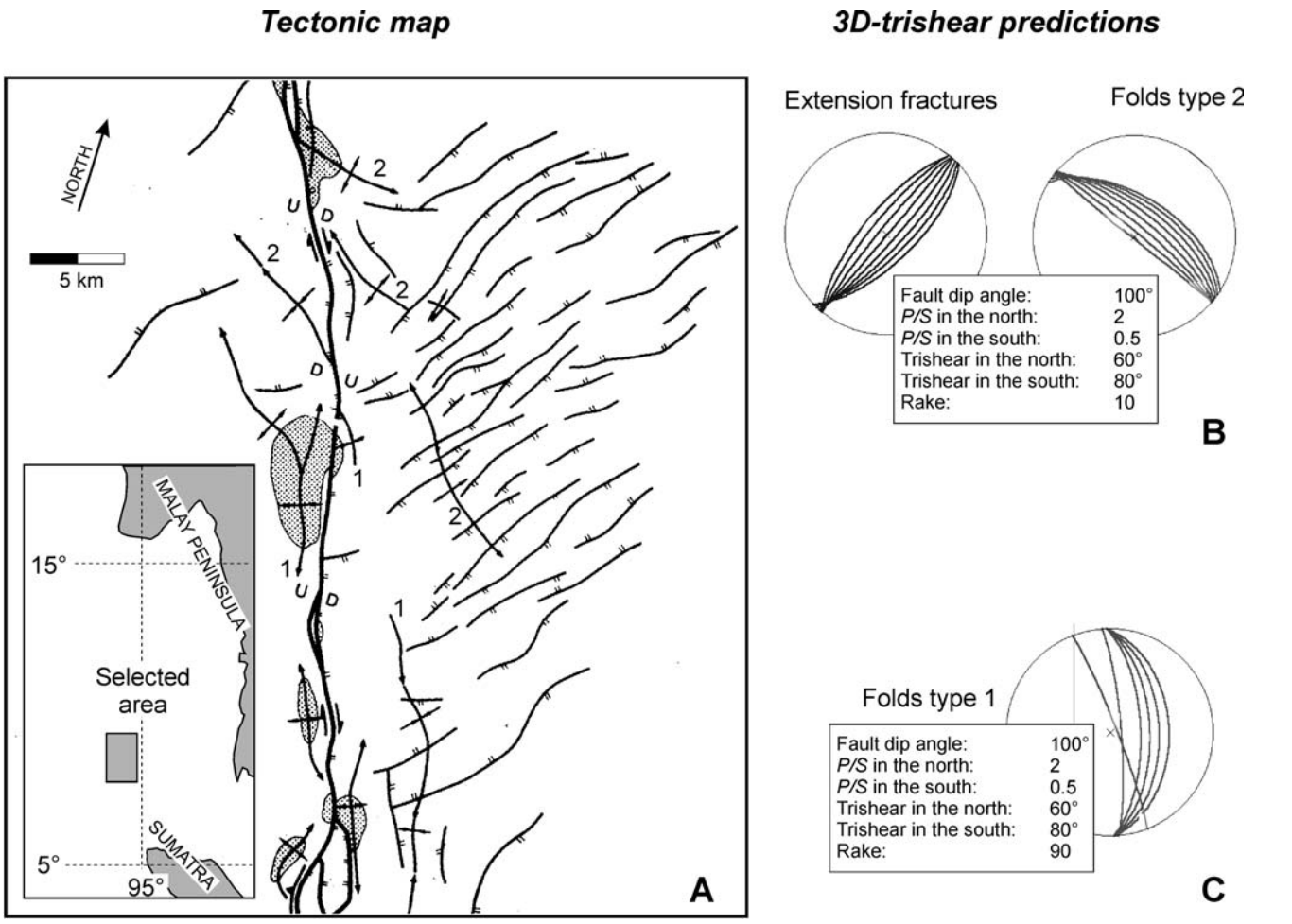

Figure 11. Comparison of the natural example of a major transform fault in the Andaman Sea described by Harding (1985) with two models of three-dimensional trishear. (A) Structural map of the region. The numbers identify the type of fold mentioned in text. (B) The oblique normal faults that flank the wrench fault and fold type 2 compare well with the predictions of a 10° rake three-dimensional trishear model. (C) To obtain fold type 1, it was necessary to construct a 90° rake model.

Two seismic profiles across the wrench fault show that the master fault has a normal separation and 80°ENE dip (Harding, 1985). These profiles, together with the horizontal displacement provided by Harding (1985), indicate the ratio of strike slip to dip slip and permitted us to calculate the rake of the master fault, 10°, and the trishear angles, 60° in the north and 80° in the south. A three-dimensional trishear model with *P*/*S* ratio varying between 2 and 0.5 from north to south was constructed to suit the different structures presented in the area.

The oblique normal faults that flank the wrench fault and type 2 folds compare well with the predictions of the three-dimensional trishear numerical model (Fig. 11). In order to obtain folds of type 1, it was necessary to construct a 90° rake model.

Example 3: Confidence Hills, California, United States

The Confidence Hills (Fig. 12) form a positive flower structure developed along the current trace of the southern Death Valley dextral strike-slip fault zone (Wright and Troxel, 1984; Troxel and Butler, 1986; Butler et al., 1988). Two overlapping and segmented dextral northwest-striking strike-slip fault systems bound the hills, and northwest- and southeast-plunging folds are located between them (Wright and Troxel, 1984; Butler et al., 1988; Dooley and McClay, 1996; see Fig. 12A). Because the fault zones are inferred by Dooley and McClay (1996) to link to a common basal vertical fault system at depth, we can simulate their interpretation with the three-dimensional trishear model. Pliocene to Holocene lacustrine and alluvial-fan sedimentary rocks are involved in the deformation. Three prominent faults are found at angles of 19° to 24° (clockwise-oblique) to one of the main faults and have been interpreted by Dooley and McClay (1996) to represent remnant Riedel shears.

To construct a three-dimensional trishear model that accounts for the fractures of the area, we used a 45° rake. We calculated a trishear angle of 30° and 60° for the northernmost and southernmost cross sections, respectively, as presented by Dooley and McClay (1996). The synthetic Riedel 1 shears of the model, presented in Figure 12B, perfectly fit the three prominent faults.

COMPARISON WITH AN ANALOGUE EXPERIMENT

Richard and Krantz (1991) performed analogue experiments on fault reactivation in

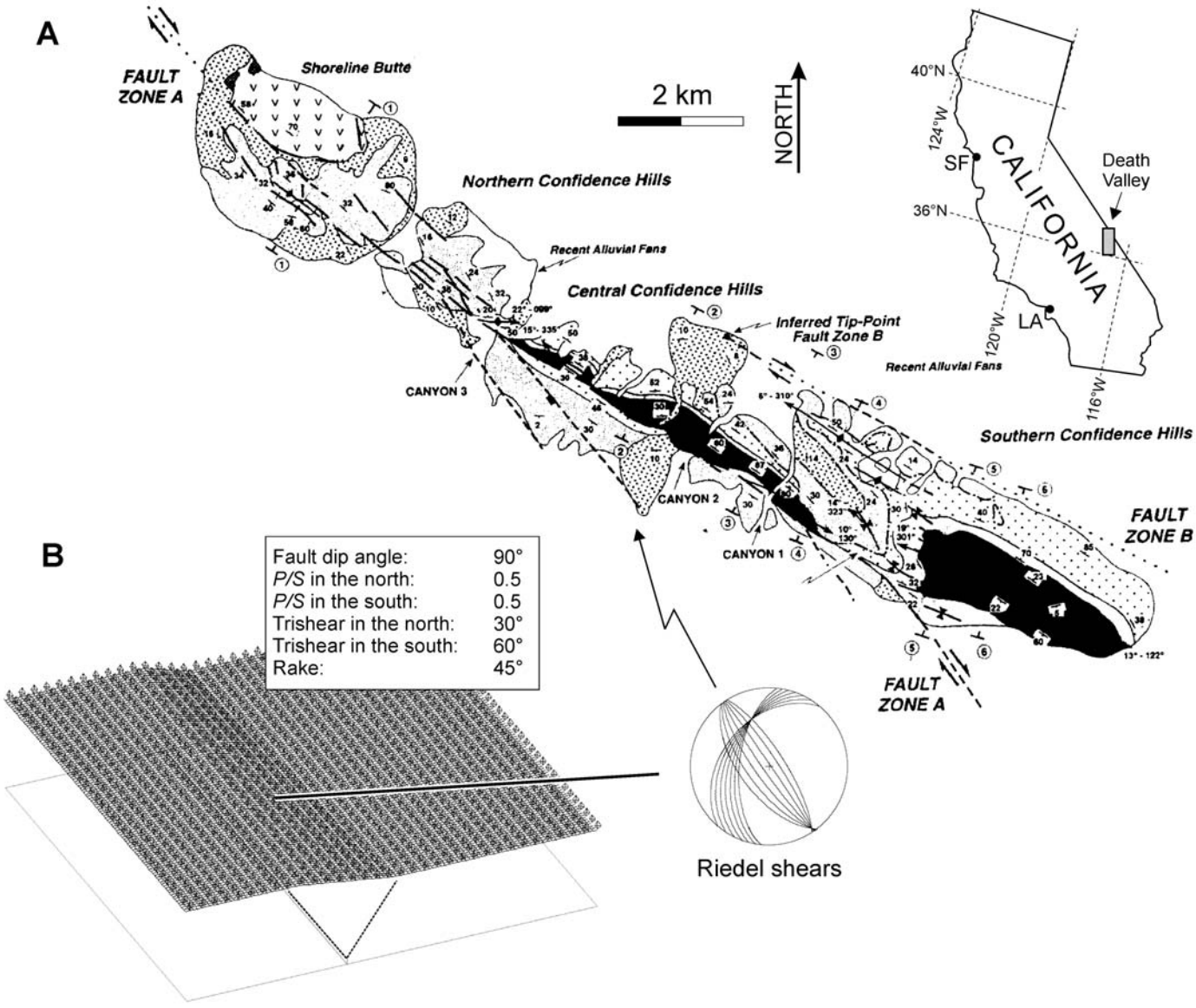

Figure 12. (A) Geologic map of the Confidence Hills and a location map, showing two dextral northwest-trending strike-slip faults systems with associated folds and fractures (Dooley and McClay, 1996). (B) Three-dimensional trishear model with a 45° rake, which accounts for the Riedel shears of the natural example. SF—San Francisco; LA—Los Angeles.

strike-slip mode: (1) a reverse basement fault dipping 54°, (2) a vertical fault, and (3) a normal fault dipping 45°. We compare the first two with predictions from the three-dimensional trishear model. In each experiment, the first stage of deformation was a pure dip-slip displacement and the second stage, which represents the reactivation in strike-slip mode, was a pure right-lateral motion. In the three-dimensional trishear model, this deformation can be simulated with rakes of 90° and 0°, respectively. For each type of fault, Richard and Krantz (1991) used three different models: (1) a pure sand layer, which provides an analogue for brittle faulting, (2) a thick sand layer overlying a thin silicone layer, and (3) a sand layer overlying a thick silicone layer, which simulates a ductile behavior. For the three-dimensional trishear model, this variation in the physical properties was achieved by changing the P/S ratio (2, 1, and 0.3, respectively). We estimated the trishear angle from the cross sections of each model given by Richard and Krantz (1991).

Experiment Involving a Reverse Fault Dipping 54°

In the three-dimensional trishear, the en echelon pattern of strike-slip faults was achieved in the three models and is represented by the Riedel fractures that strike 10° to 20° clockwise-oblique to the basement fault (Fig. 13). In the $P/S = 1$ and $P/S = 2$ models, as in the analogue models, the deformation was localized in a narrow band in the hanging wall (Figs. 13A and 13B). Very similar to the analogue models, we noticed that the lower the

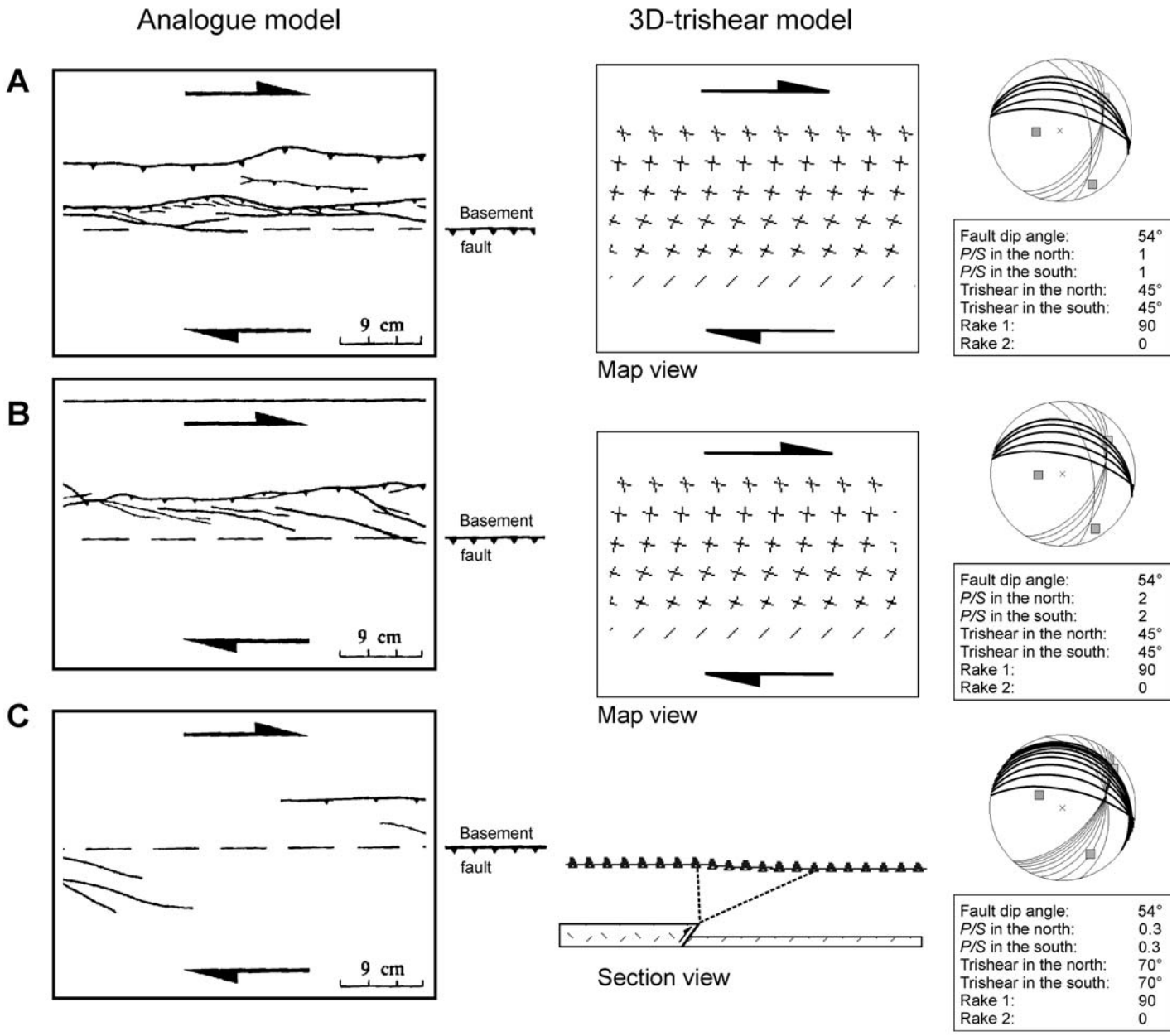

Figure 13. Comparisons between the analogue models of reactivation in pure strike-slip mode of a reverse basement fault dipping 54° performed by Richard and Krantz (1991) and the three-dimensional trishear models. (A) A $P/S = 2$ model that simulates Richard and Krantz's pure brittle experiment. (B) A $P/S = 1$ model that corresponds to Richard and Krantz's experiment involving sand overlying a thin silicone layer. (C) A $P/S = 0.3$ model that simulates Richard and Krantz's experiment involving sand overlying a thick silicone layer.

P/S ratio, the larger the angle that the Riedel shears deviated from the basement fault. Riedel shears in the $P/S = 0.3$ model, as in the analogue model, have a wider range of azimuths (Fig. 13C).

Experiment Involving a Fault Dipping 90°

The three-dimensional trishear models display close geometric similarities to the analogue models with a vertical fault developed by Richard and Krantz (1991). As in the analogue case, three models in which the P/S is 2, 1, and 0.3, respectively (see 7.1 for reference), have been considered (Figs. 14A–14C). In the first two, all of the strike-slip deformation has been restricted to a narrow zone (Figs. 14A and 14B). In the $P/S = 0.3$ model, we obtained a similar shift toward the uplifted block (Fig. 14C). In cross section, the geometry of the faults fits well with the analogue model (Fig. 15).

DISCUSSION

Our kinematic algorithm is simple and at present only permits linear variations of some parameters such as P/S ratio and trishear apical angle. More complex models can be devised to analyze other nonlinear cases and to incorporate some mechanical observations. However, the utility of this kind of forward method is to obtain some

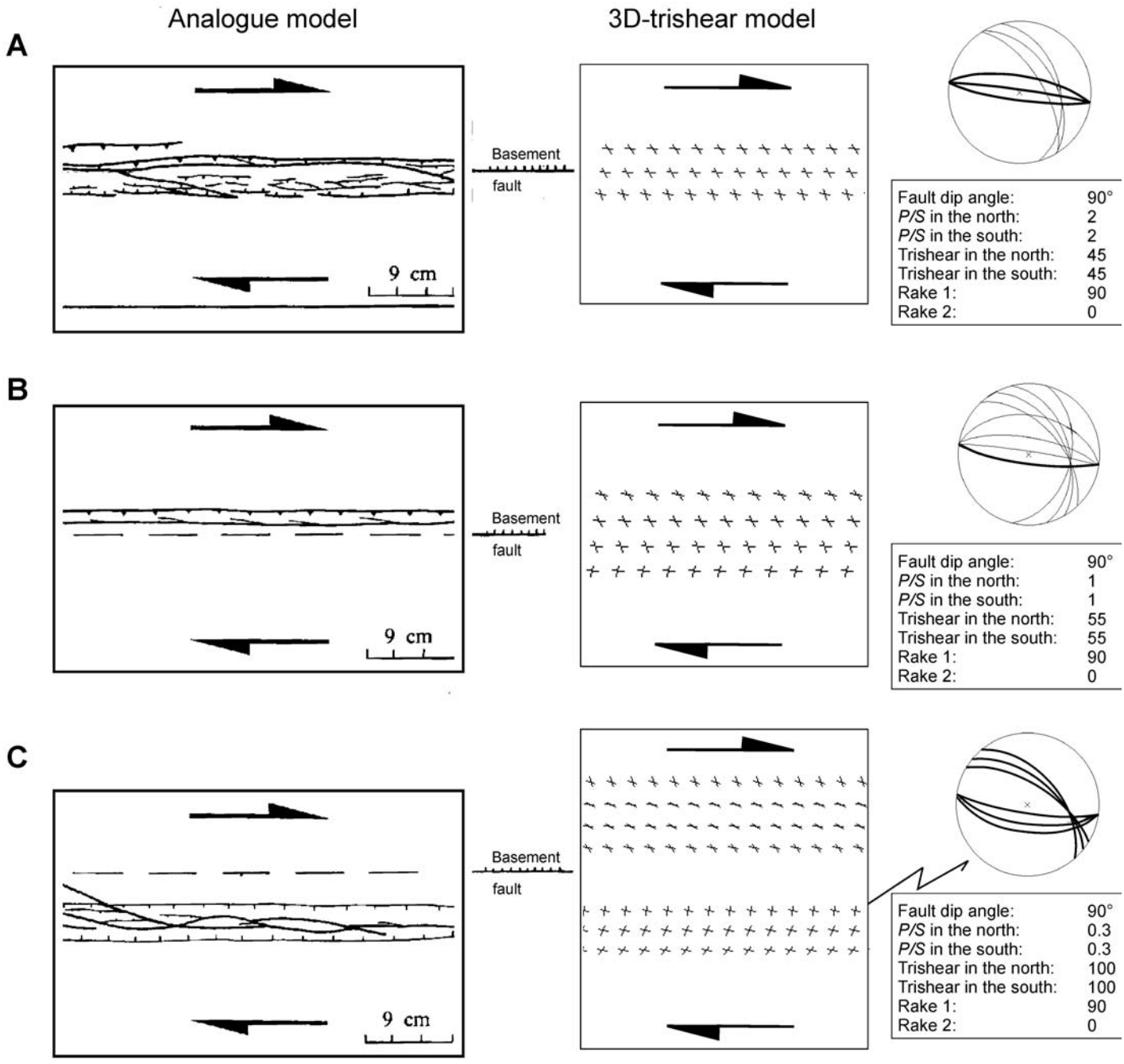

Figure 14. Comparisons between the analogue models of reactivation in pure strike-slip mode of a basement fault dipping 90° performed by Richard and Krantz (1991) and the three-dimensional trishear models. (A, B, and C) The *P*/*S* = 2, 1, and 0.3 models simulate the experiments using pure brittle sand overlying a thin silicone layer, and sand overlying a thick silicone layer, respectively.

general ideas and some general predictions because it is very difficult to fit by trial and error a numerical model to a natural example. Unfortunately, the inverse method proposed by Allmendinger (1998) for the two-dimensional trishear model would be extremely time-consuming to analyze for a three-dimensional case.

Because of this limitation, we suggest that the most important results of three-dimensional trishear modeling are to allow visualization of the intensity and orientation of deformation for any three-dimensional position and to predict, in a general way, some patterns of fracture curvatures and how they vary with the obliquity of the displacement. The sophistication of the algorithm will be superfluous until the development of a relatively fast inverse method, which could increase the utility of the model.

CONCLUSIONS

The algorithm proposed here for three-dimensional trishear is less versatile than the

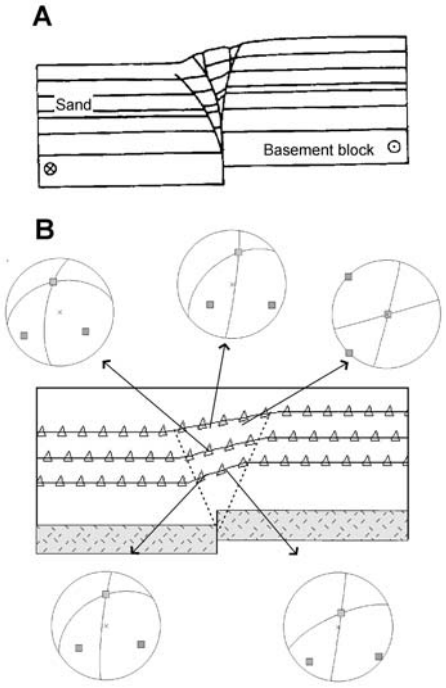

Figure 15. (A) Cross section of the reactivation in pure strike-slip mode of a basement fault dipping 90° (Richard and Krantz, 1991). (B) Three-dimensional trishear model consistent with the analogue model. The stereographic projections show the predicted Riedel shear faults.

pseudo–three-dimensional algorithm presented by Cristallini and Allmendinger (2001) for dip-slip deformation but is much more powerful for analyzing oblique-slip and strike-slip systems. Changes of slip, *P*/*S* ratio, and trishear apical angle can be made along the strike of the main fault, and any obliquity of the displacement is allowed. The strain ellipsoid can be derived for any point inside the model, and the orientation of shear and extensional fractures can be predicted.

A basic analysis of strike-slip deformation made with three-dimensional trishear modeling simulated helicoidal fractures observed in strike-slip–related structures. More complex configurations with oblique slip and variations along strike can explain a wide range of minor structures.

The model successfully reproduces, in a general way, the geometry of faults, folds, and fractures described in natural strike-slip systems including positive and negative flower structures. It also resembles analogue models of fault reactivation in strike-slip mode.

Important limitations to the three-dimensional trishear model must be considered when applying it to studies of natural structures. Nevertheless, the usefulness of the model in understanding the deformation is well demonstrated by the strong similarities between the results and the natural examples described in this paper.

ACKNOWLEDGMENTS

This research was supported by grants from the Fundación Antorchas (Reentry Grant), UBACYT [x914], and PICT99-6729 to Cristallini and National Science Foundation (grants EAR-9814348 and EAR-0125557) to Allmendinger. Acknowledgment is also made to the Consejo Nacional de Investigaciones Científicas y Técnicas (CONICET) of Argentina, Universidad de Buenos Aires, and Cornell University. Discussions with Néstor Cardozo and reviews by Eric Erslev, Stuart Hardy, and Associate Editor Wanda Taylor have greatly improved this paper.

REFERENCES CITED

Allmendinger, R.W., 1998, Inverse and forward modeling of trishear fault-propagation folds: Tectonics, v. 17, p. 640–656.

Butler, P.R., Troxel, B.W., and Verosub, K.L., 1988, Late Cenozoic history and style of deformation along the southern Death Valley fault zone, California: Geological Society of America Bulletin, v. 100, p. 402–410.

Cardozo, N., Bhalla, K., Zehnder, A., and Allmendinger, R., 2003, Mechanical models of fault propagation folds and comparison to the trishear kinematic model: Journal of Structural Geology, v. 25, p. 1–18.

Cristallini, E.O., and Allmendinger, R.W., 2001, Pseudo 3-D modeling of trishear fault-propagation folding: Journal of Structural Geology, v. 23, p. 1883–1899.

Dooley, T., and McClay, K., 1996, Strike-slip deformation in the Confidence Hills, southern Death Valley fault zone, eastern California, USA: Geological Society [London] Journal, v. 153, p. 375–387.

Dooley, T., and McClay, K., 1997, Analogue modeling of pull-apart basins: American Association of Petroleum Geologists Bulletin, v. 81, p. 1804–1826.

Erslev, E.A., 1991, Trishear fault-propagation folding: Geology, v. 19, p. 617–620.

Finch, E., Hardy, S., and Gawthorpe, R., 2003, Discrete element modelling of contractional fault-propagation folding above rigid basement fault blocks: Journal of Structural Geology, v. 25, p. 515–528.

Harding, T.P., 1985, Seismic characteristics and identification of negative flower structures, positive flower structures, and positive structural inversion: American Association of Petroleum Geologists Bulletin, v. 69, p. 582–600.

Hardy, S., and Ford, M., 1997, Numerical modeling of trishear fault propagation folding: Tectonics, v. 16, p. 841–854.

Johnson, K., and Johnson, A., 2002, Mechanical models of trishear-like folds: Journal of Structural Geology, v. 24, p. 277–287.

Mase, G.E., and Mase, G.T., 1992, Continuum mechanics for engineers: Boca Raton, Florida, CRC Press, p. 377.

Naylor, M.A., Mandl, G., and Sijpesteijn, C.H.K., 1986, Fault geometries in basement-induced wrench faulting under different initial stress states: Journal of Structural Geology, v. 8, p. 737–752.

Reches, Z., 1978, Analysis of faulting in three-dimensional strain field: Tectonophysics, v. 47, p. 109–129.

Richard, P., and Krantz, R.W., 1991, Experiments on fault reactivation in strike-slip mode: Tectonophysics, v. 188, p. 117–131.

Roussos, N., and Triantafyllos, L., 1991, Structure of the central North Aegean Trough: An active strike-slip deformation zone: Basin Research, v. 3, p. 39–48.

Sylvester, A.G., 1988, Strike-slip faults: Geological Society of America Bulletin, v. 100, p. 1666–1703.

Tindall, S.E., and Davis, G.H., 1999, Monocline development by oblique-slip fault-propagation folding: The East Kaibab monocline, Colorado Plateau, Utah: Journal of Structural Geology, v. 21, p. 1303–1320.

Troxel, B.W., and Butler, P.R., 1986, Multiple Quaternary deformation central of the Confidence Hills, Death Valley, California: An example of folding along a strike-slip fault zone, *in* Troxel, B.W., ed., Quaternary tectonics of southern Death Valley, California: Field trip guide: Shoshone, California, B.W. Troxel Publications, p. 25–28.

Vergani, G.D., Tankard, A.J., Belotti, H.J., and Welsink, H.J., 1995, Tectonic evolution and paleogeography of the Neuquén Basin, Argentina, *in* Tankard, A.J., et al., eds., Petroleum basins of South America: American Association of Petroleum Geologists Memoir 62, p. 383–402.

Williams, G.D., and Kane, S.J., 1999, Three dimensional restoration algorithm and finite strain in thrust systems, *in* Thrust tectonics 99 Conference Programme: London, UK, University of London, p. 32–34.

Woodcock, N.H., and Fischer, M., 1986, Strike-slip duplexes: Journal of Structural Geology, v. 8, p. 725–735.

Woodcock, N.H., and Schubert, C., 1994, Continental strike-slip tectonics, *in* Hancock, P.L., ed., Continental deformation: Oxford, Pergamon Press, p. 251–263.

Wright, L.A., and Troxel, B.W., 1984, Geology of the northern half of the Confidence Hills 15 minute quadrangle Death Valley region, eastern California: The area of the Amargosa Chaos: California Division of Mines and Geology Map Sheet 34, scale 1:24,000.

Zehnder, A.T., and Allmendinger, R.W., 2000, Velocity field for the trishear model: Journal of Structural Geology, v. 22, p. 1009–1014.

Manuscript Received by the Society 10 October 2002
Revised Manuscript Received 14 June 2003
Manuscript Accepted 9 October 2003

Printed in the USA